JACS
JOURNAL OF THE AMERICAN CHEMICAL SOCIETY
Article
pubs.acs.org/JACS

Solvent-Mediated Crystallization of $CH_3NH_3SnI_3$ Films for Heterojunction Depleted Perovskite Solar Cells

Feng Hao,[†] Constantinos C. Stoumpos,[†] Peijun Guo,[‡] Nanjia Zhou,[‡] Tobin J. Marks,[†] Robert P. H. Chang,[‡] and Mercouri G. Kanatzidis*[,†]

[†]Department of Chemistry and [‡]Department of Materials Science and Engineering, and Argonne-Northwestern Solar Energy Research (ANSER) Center, Northwestern University, 2145 Sheridan Road, Evanston, Illinois 60208, United States

Supporting Information

ABSTRACT: Organo-lead halide perovskite solar cells have gained enormous significance and have now achieved power conversion efficiencies of ~20%. However, the potential toxicity of lead in these systems raises environmental concerns for widespread deployment. Here we investigate solvent effects on the crystallization of the lead-free methylammonium tin triiodide ($CH_3NH_3SnI_3$) perovskite films in a solution growth process. Highly uniform, pinhole-free perovskite films are obtained from a dimethyl sulfoxide (DMSO) solution via a transitional SnI_2·3DMSO intermediate phase. This high-quality perovskite film enables the realization of heterojunction depleted solar cells based on mesoporous TiO_2 layer but in the absence of any hole-transporting material with an unprecedented photocurrent up to 21 mA cm^{-2}. Charge extraction and transient photovoltage decay measurements reveal high carrier densities in the $CH_3NH_3SnI_3$ perovskite device which are one order of magnitude larger than $CH_3NH_3PbI_3$-based devices but with comparable recombination lifetimes in both devices. The relatively high background dark carrier density of the Sn-based perovskite is responsible for the lower photovoltaic efficiency in comparison to the Pb-based analogues. These results provide important progress toward achieving improved perovskite morphology control in realizing solution-processed highly efficient lead-free perovskite solar cells.

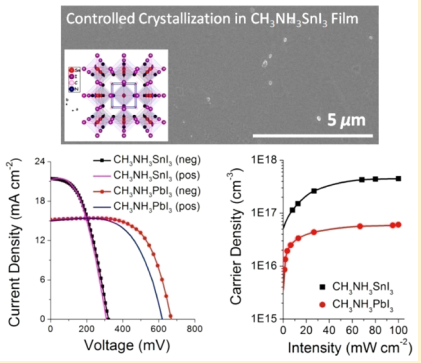

INTRODUCTION

The recent emergence of organic−inorganic halide hybrid perovskite-based solar cells has evoked widespread interest in both scientific and industrial communities, primarily because of the high power conversion efficiencies coupled with a relatively simple and scalable processing techniques.[1−4] These compounds are part of the ABX_3 perovskite family and consist of a network of corner-sharing BX_6 octahedra, where the B atom is a divalent metal cation (typically Ge^{2+}, Sn^{2+}, or Pb^{2+}) and X is a monovalent anion (typically halides of F^-, Cl^-, Br^-, or I^-); the A cation balances the negative charge, and it can be a Cs^+ or a small molecular species (such as methylammonium or formamidium).[5−8] Such perovskites have excellent optical properties that are tunable by controlling the chemical compositions[9,10] and exhibit facile ambipolar charge transport[11] and long electron and hole diffusion lengths.[12,13] Various device structures have been realized ranging from the sensitized solar cells on mesoporous TiO_2 scaffolds[11] or insulating Al_2O_3 underlayers[14,15] to the planar heterojunction architectures[16,17] and hole-transporting material-free depleted heterojunction devices.[18−20] Solar cells based on the benchmark $CH_3NH_3PbI_3$ perovskites have reached confirmed power conversion efficiencies up to 20%[15,21−23] and thus have rapidly surpassed the efficiencies of many other emerging and commercial photovoltaics.[24−26]

It is becoming increasing evident, however, that it would be highly desirable to achieve analogous optical and photovoltaic performance using *lead-free* organic−inorganic perovskite compounds because of the anticipated toxicity from a potentially soluble lead source. Recently, we and other groups have reported that the methylammonium tin iodide ($CH_3NH_3SnI_3$) analogue could serve as a lead-free light-absorbing material, and solar cell power conversion efficiencies in the range of 5−6% have been obtained independently.[10,27] However, the efficiency obtained is well below that of the lead counterpart, and it is believed that this originates from the self-doping of the tin perovskite due to the facile conversion of Sn^{2+} to the Sn^{4+} oxidation state. This process generates p-type carriers and results in limited diffusion lengths for the photoexcited carriers.[27] The film quality (such as homogeneity and coverage) of the $CH_3NH_3SnI_3$ perovskite layer is another limiting factor governing the device photovoltaic performance.[10] The poor film coverage with the presence of micron-size pinholes is related to an uncontrollable crystallization during the solution-based deposition process, a behavior which is notably different from the lead analogue.[28] The reaction between the SnI_2 films and methylammonium iodide is recognized to be much faster than for the Pb analogue.[29] The

Received: June 26, 2015

DOI: 10.1021/jacs.5b06658
J. Am. Chem. Soc. XXXX, XXX, XXX−XXX

easy decomposition of the tin perovskite in isopropanol solvent also makes the sequential solution process difficult to realize.[22] Therefore, developing novel deposition methods for high-quality $CH_3NH_3SnI_3$ films which are expected to achieve an efficiency boost in the development of lead-free perovskite solar cells remains a challenge.

Compared to the numerous studies on the morphological control of $CH_3NH_3PbI_3$ film growth,[16,22,23,30−33] studies on the tin counterparts are sparse because experiments are typically hampered by rapid oxidation under ambient conditions and the requirement of an inert dry atmosphere. Here we show that the crystallization of the $CH_3NH_3SnI_3$ perovskite films can be greatly improved through solvent engineering employed in a one-step spin-coating process. Solvent evaporation effects are detrimental to obtaining high-quality $CH_3NH_3SnI_3$ films given the faster reaction rate between the two halide precursors compared to the $CH_3NH_3PbI_3$ analogue. Controlled solvent evaporation and the convective self-assembly process during spin-coating effectively induce the formation of well-crystallized $CH_3NH_3SnI_3$ perovskite films due to the high enthalpy of crystallization, which is much greater than the solvation energies of the individual ions. Here we report that very uniform, pinhole-free $CH_3NH_3SnI_3$ perovskite films can be obtained from a strongly coordinating solvent such as dimethyl sulfoxide (DMSO) which stabilizes a transitional SnI_2·3DMSO intermediate phase. Crystallization processes using other highly polar solvents, *N*,*N*-dimethylformamide (DMF) and *N*-methyl-2-pyrrolidone (NMP), have also been investigated and are compared here. Taken together, these results show that solvated intermediates are an important transitional step toward a uniform, high-coverage perovskite films. Benefiting from the high-quality of the present $CH_3NH_3SnI_3$ films, lead-free perovskite heterojunction depleted solar cells are fabricated with photocurrent densities of up to 21 mA cm^{-2}, albeit with a relatively modest diffusion length. The underlying carrier generation, electron transfer, and recombination dynamics are investigated and compared by charge extraction and small perturbation transient photovoltage analyses in both methylammonium tin and lead halide perovskite devices. We show that the carrier density in the $CH_3NH_3SnI_3$ perovskite device is one order of magnitude larger than that of the lead analogue, but the recombination lifetimes in both devices are comparable. Our results hold promise for further efficiency enhancement in lead-free perovskite solar cells, taking advantage of higher quality perovskite films.

RESULTS AND DISCUSSION

Film Fabrication and Characterization. The selection of solvents for dissolving tin halide perovskites is found to be critical for obtaining high quality thin films using solution coating techniques. In general, the choice of solvent is a balance between several competing factors. On the one hand, the solvent must be capable of dissolving both the inorganic and organic halide components, and therefore a good choice of solvent can be found among the strongly coordinating/polar amide class. On the other hand, if the reagent solubility in the solvent is too high, then during the deposition of successive layers previous layers will redissolve during the deposition of the next layer.[6] Normally, γ-butyrolactone (GBL), dimethyl sulfoxide (DMSO), *N*-methyl-2-pyrrolidone(NMP), and *N*,*N*-dimethylformamide (DMF) are widely used for lead halides and methylammonium iodide.[29] The basic physical properties of these solvents are summarized in Table 1 for comparison.

Table 1. Physical Properties of the Polar Solvents Used in the Perovskite Film Deposition[64]

	boiling point (°C)	viscosity (cP)	dielectric constant	vapor pressure at 20 °C (Torr)
DMF	152	0.92	36.7	2.7
GBL	204	1.90	39.1	1.5
NMP	202	1.65	33	0.29
DMSO	189	2.00	46.7	0.42

One of the fundamental challenges encountered in the one-step tin perovskite spin-coating process is that a homogeneous perovskite layer cannot be formed over a large area, even when a convective spreading flow due to centrifugal force is applied to the slowly evaporating solvents.[34] Note that for identical concentrations, $CH_3NH_3SnI_3$ solutions crystallize much more rapidly than those of $CH_3NH_3PbI_3$ when DMF is the solvent. This is readily evidenced by the spontaneous formation of a black perovskite layer after the spin-coating process in the case of $CH_3NH_3SnI_3$, whereas the complete crystallization of $CH_3NH_3PbI_3$ is much slower and is achieved only on thermal treatment. This difference stems from the faster reaction of SnI_2 with CH_3NH_3I to form the perovskite, owing to the greater Lewis acidity of Sn^{2+} versus Pb^{2+}.[35] Therefore, retardation of the crystallization process is considered here to be beneficial for better $CH_3NH_3SnI_3$ film quality since the perovskite is allowed to form in a stepwise, controllable fashion. Compared to the routinely used DMF, DMSO has a higher coordination affinity, a relatively high boiling point (189 °C), and a low saturated vapor pressure (0.42 Torr at 20 °C). Several recent studies have confirmed that the strong coordination of $CH_3NH_3PbI_3$ by DMSO leads to stabilization of intermediate solvated compounds.[30,35] On the other hand, the viscosity of the solvent is also important in controlling evaporation during the spin-coating process and should be taken into consideration during homogeneous thin-film fabrication. From the above considerations, DMF and DMSO were selected to fabricate $CH_3NH_3SnI_3$ films and to compare their crystallization processes.

A mesoporous TiO_2 layer with a thickness of 200 nm was used as the substrate for all perovskite depositions in this study. Perovskite films were deposited using a one-step spin-coating process from 1.0 M perovskite solutions. It was immediately clear that the different solvents markedly affect the resultant perovskite film formation. As stated above and shown in Figure 1a, $CH_3NH_3SnI_3$ perovskite crystals form immediately during the spin-coating process from DMF, as evidenced from the color changing to dark brown during 4000 rpm rotation without any thermal treatment. Switching to DMSO effectively slows the perovskite crystallization since the color change to dark brown is not observed during spin-coating. The coated layer from DMSO solvent is uniform and light yellow. A black perovskite film gradually forms when annealing the substrate at 100 °C on a preheated hot plate for 15 min. To understand the solvent effects on the perovskite crystallization process, X-ray diffraction (XRD) patterns of the films before and after the thermal annealing process were analyzed. As shown in Figure 1b, the as-cast films from DMF show high crystallinity regardless of the thermal annealing, and all the peaks can be indexed to the tetraganol $CH_3NH_3SnI_3$ phase in space group *P*4*mm*. This high crystallinity underscores the rapid perovskite crystallization during spin-coating from DMF solution. However, when DMSO was used as the solvent, the as-formed

DOI: 10.1021/jacs.5b06658
J. Am. Chem. Soc. XXXX, XXX, XXX−XXX

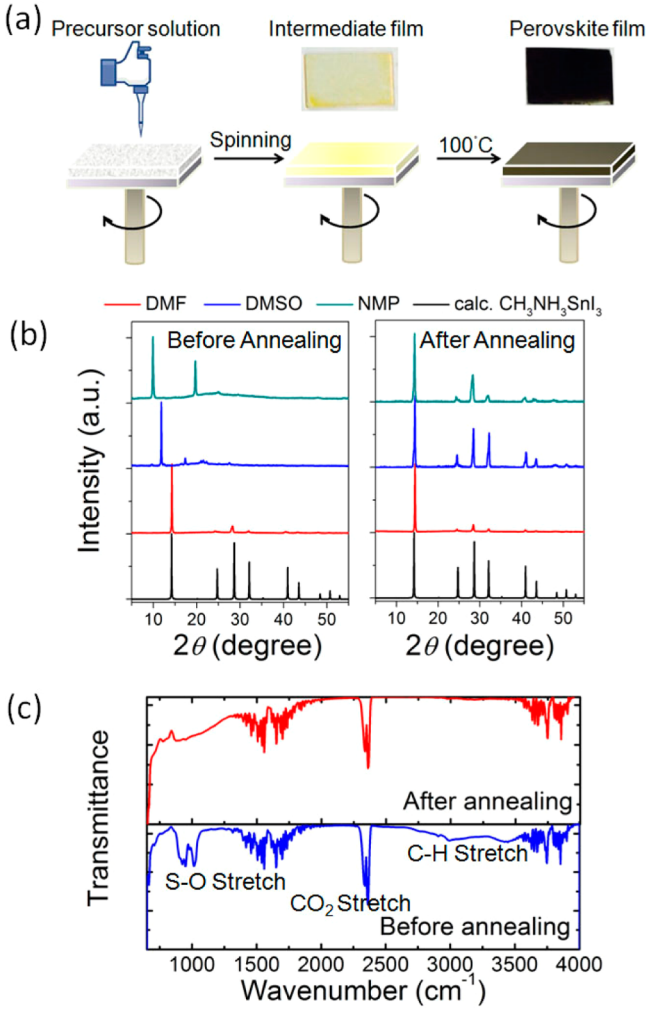

Figure 1. (a) Single step spinning-coating process with the formation of DMSO solvate intermediate. Images of the as-prepared films from a DMSO solution before and after annealing process are shown in the insets. (b) X-ray diffraction patterns of the perovskite layer with different solvents before (left) and after (right) thermal annealing process at 100 °C for 15 min. (c) FTIR spectra of the perovskite layer deposited from DMSO solution before annealing showing the characteristic C−S and C−O stretching vibrations from the Sn^{2+}-coordinated DMSO solvent at 960 and 1012 cm^{-1}, respectively. Upon annealing, these characteristic DMSO peaks disappear, confirming the complete removal of the solvent and conversion of the intermediate compound to the $CH_3NH_3SnI_3$ perovskite.

films show a totally different set of reflections, which cannot be assigned either to the starting precursor or the target perovskite compound. We therefore assume this is an intermediate solvated phase formed during the perovskite deposition process. Previous reports have shown that DMSO forms a $CH_3NH_3PbI_3$·DMSO complex.[32,36] In the present system, the formation of the intermediate phase can be observed from the XRD features at lower angles. Unlike the case of $CH_3NH_3PbI_3$·DMSO, however, where reflections analogous to our previously reported $CH_3NH_3PbI_3$·DMF and $CH_3NH_3PbI_3$·H_2O solvates were observed,[28] in the case of the tin perovskite an intermediate solvated phase does not contain the $CH_3NH_3^+$ cation and has been identified as SnI_2·3DMSO. Note that the Sn solvate has a completely different crystal structure than that of formally analogous PbI_2·2DMSO.[36] The presence of the DMSO solvate phase indicates that the formation of the $CH_3NH_3SnI_3$ perovskite is dramatically inhibited by the strong solvent coordination to the metal precursor.

The presence of DMSO in the intermediate phase was further confirmed by Fourier transform infrared spectroscopy (FTIR). Figure 1c shows the FTIR spectra of the characteristic C−S and S−O stretching vibrations from the Sn^{2+}-coordinated DMSO solvent at 960 and 1012 cm^{-1}, respectively. Upon annealing, these characteristic modes of the DMSO molecule disappear, thus confirming the complete removal of the solvent and the conversion of the intermediate compound to the $CH_3NH_3SnI_3$ perovskite. For comparison, the characteristic C═O bonding of the DMF solvent is absent in the perovskite film fabricated from DMF, as shown in Figure S1. The crystal structure of the solvent-induced intermediate was further characterized by single crystal X-ray diffraction. Pale yellow block crystals of SnI_2·3DMSO were obtained by means of the a recently reported antisolvent vapor-assisted crystallization process,[37] using 1.0 mL of a 2.0 M DMSO solution of $CH_3NH_3SnI_3$ with CH_2Cl_2 as the antisolvent. The crystal structure was solved by direct methods and refined using SHELXTL software.[38] As shown in Figure 2a, the crystal structure of SnI_2·3DMSO is composed of discrete $SnI(DMSO)_3^+$ ions in a seesaw coordination environment. Three O-coordinated DMSO molecules occupy the corners of a trigonal pyramid with the Sn ion at the apex, and a fourth iodide ion completes the coordination sphere. The seesaw polyhedra are linked by a nearly free I^- ion which coordinates via weak (3.522 Å) or very weak (3.987 Å) bonding interactions. The incorporation of all three iodide ligands changes the coordination of the Sn to octahedral with the O atoms (DMSO) and the three loosely bound iodide atoms occupying opposing facial positions. This self-assembly results in the formation of 1D zigzag chains running down the crystallographic *b*-axis (Figure 2b). Structural details can be found in the Supporting Information. It is instructive to note here that the present film formation process through solvent engineering is markedly different in $CH_3NH_3PbI_3$ and $CH_3NH_3SnI_3$ with DMSO. Whereas in the former case the DMSO film acts as a hydrogen bond acceptor in $CH_3NH_3PbI_3$·DMSO (assuming a similar structure to $CH_3NH_3PbI_3$·DMF), in the latter case DMSO directly coordinates to the Sn ion in SnI_2·3DMSO, leaving the $CH_3NH_3^+$ cation dissolved in the mother liquor (Figure 2c). Thus, perovskite formation takes place on the substrate, and the perovskite film formation can be controlled by varying the rate of DMSO evaporation.

NMP was also investigated as a solvent to further understand the effect of the intermediate phase on the tin perovskite formation process. As DMSO, NMP is a polar aprotic solvent with a high boiling point of 202 °C and low vapor pressure (0.29 Torr at 20 °C). Similar to DMSO, the NMP forms black perovskite film only after annealing of the spin-cast film at 100 °C. The color change from pale yellow to black takes place more slowly than from DMSO. We attribute this to the slightly higher boiling point of NMP and slower release of the coordinated solvent on thermal treatment. As demonstrated in Figure 1a, X-ray diffraction of the as-cast NMP pale yellow films shows very different features from the black $CH_3NH_3SnI_3$ phase. The characteristic peak at 10° suggests a larger unit cell for the solvated phase, which may be ascribed to the larger volume of NMP incorporated compared to DMSO. GBL was also examined for comparison in this study. It was noticed the crystallization rate of the perovskite film from GBL solvent is faster than from DMSO and NMP, but slower than DMF. The

DOI: 10.1021/jacs.5b06658
J. Am. Chem. Soc. XXXX, XXX, XXX−XXX

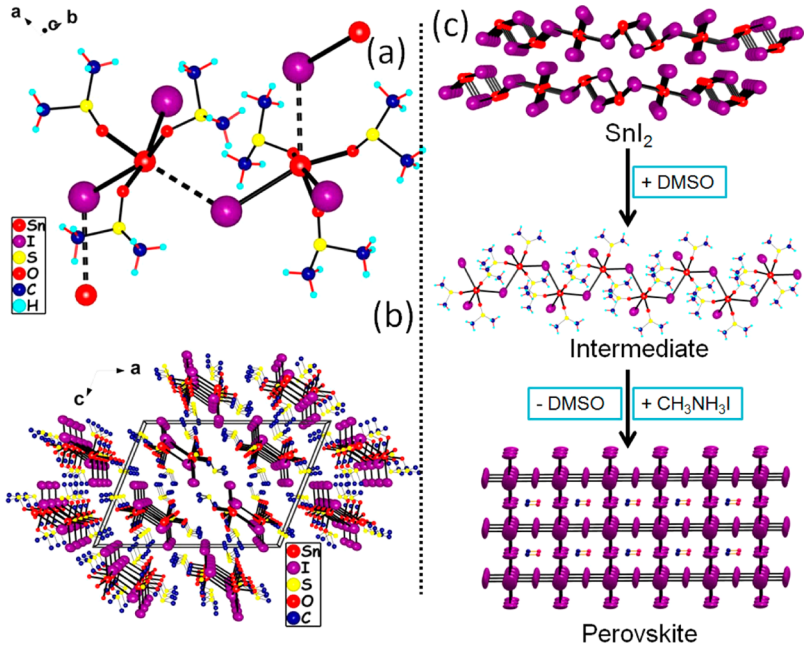

Figure 2. Crystal structure of SnI_2·3DMSO, an intermediate compound in the $CH_3NH_3SnI_3$ film fabrication process. (a) The dimeric structure of the $SnI(DMSO)_3^+$ ions linked through the lone I^- ions. (b) The unit cell of SnI_2·3DMSO in parallel view. Space group $C2/c$; a = 21.9920(10) Å, b = 10.7497(6) Å, c = 16.0302(7) Å β = 111.838(3)°. Sn−I(1) = 3.285 Å, Sn−I(2) = 3.522 Å, Sn···I(2)′ = 3.987 Å (structure details are given in the Supporting Information). (c) A schematic on the film formation of the $CH_3NH_3SnI_3$ perovskite film starting from SnI_2 through the SnI_2·3DMSO intermediate.

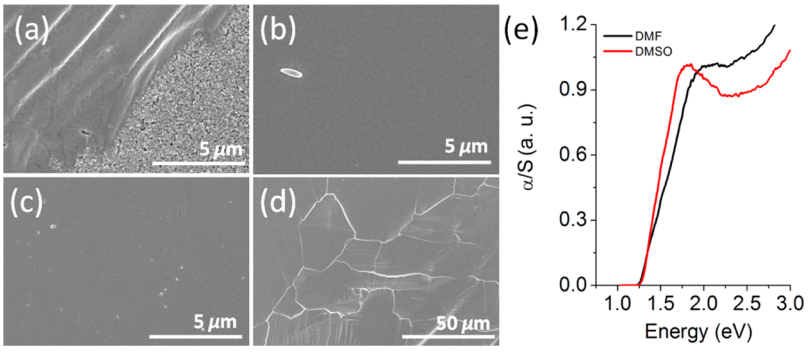

Figure 3. Representative SEM images of the as-obtained $CH_3NH_3SnI_3$ perovskite layer on mesoporous TiO_2 from different solvents, (a) DMF, (b) NMP, and (c, d) DMSO with different magnifications, and the corresponding optical absorption spectra (e). Apparently, films deposited from NMP and DMSO solvents showed complete surface coverage, whereas obvious uncovered TiO_2 surface is exposed when cast from the DMF as the solvent.

black perovskite film forms in seconds after finishing the spinning process without any heat treatment. The above trends appear to originate from the differences in evaporation rates of these three solvents during the spin-coating process. The vapor pressure at 20 °C for GBL is 1.5 Torr as listed in Table 1, which lies in between DMF (2.7 Torr) and DMSO (0.42 Torr) or NMP (0.29 Torr).

On the basis of the above observations, we propose a plausible mechanism for the formation of the uniform, high-coverage perovskite layer during the present single step spin-coating procedure. As shown in the Figure 2c, the formation of the $CH_3NH_3SnI_3$ proceeds in a controllable manner through the SnI_2·3DMSO intermediate which allows the iodide ions to react with SnI_2 in a controlled manner that is governed by the rate of the DMSO removal as a function of temperature. Therefore, a close relationship appears to exist between the solvent-induced intermediate phase and the control of the resultant perovskite film crystallization process.

Analysis of these perovskite films prepared from different solvents by scanning electron microscopy (SEM) reveals strikingly different morphologies. As compared in Figure 3, films produced from DMF solution are quite discontinuous and composed of large $CH_3NH_3SnI_3$ grains and many unfilled pinholes. This morphology arises from relatively fast crystallization rate resulting from the high nucleation rate during the drying process. Employing a solvent with lower vapor pressure than DMF, such as GBL solvent gives improved film coverage but still has pinholes as presented in Figure S3. In contrast, films deposited from DMSO as the solvent are homogeneous with almost full surface coverage on the mesoporous TiO_2 layer. Impressively, this very smooth $CH_3NH_3SnI_3$ layer shows large micron-sized grains, which is a highly desirable property, as shown in recent studies where the photovoltaic performance of the benchmark $CH_3NH_3PbI_3$ solar cells was investigated as a function of grain size.[39] The normalized optical absorption spectra of the perovskite films derived from different solvents in

DOI: 10.1021/jacs.5b06658
J. Am. Chem. Soc. XXXX, XXX, XXX−XXX

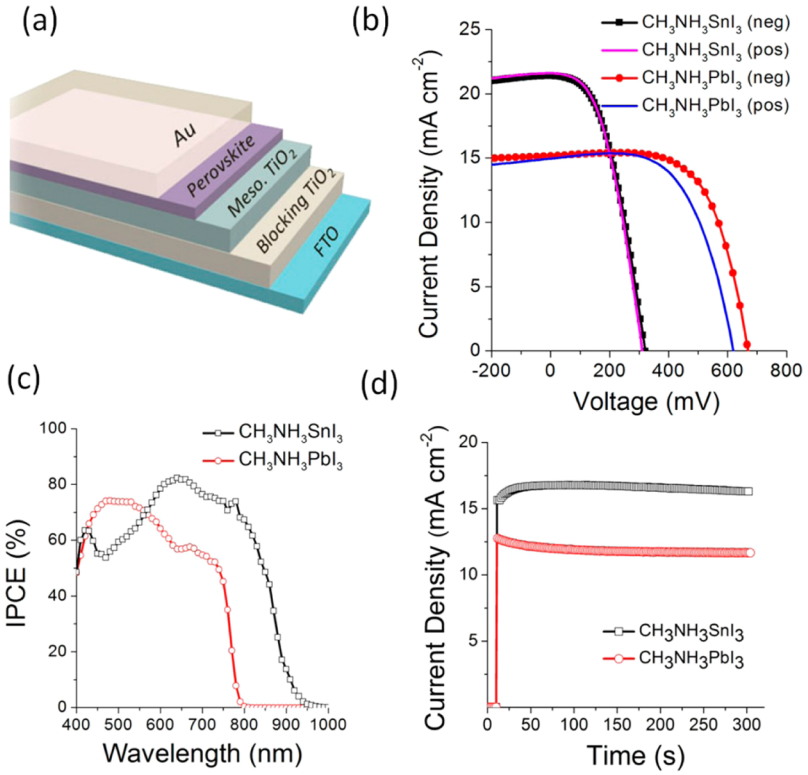

Figure 4. (a) Device architecture of the depleted heterojunction perovskite solar cell (FTO glass/blocking TiO_2 layer/mesoporous TiO_2 layer/perovskite/Au). (b) Characteristic photocurrent−voltage plots and (c) incident photon-to-current efficiency (IPCE) spectra for the $CH_3NH_3SnI_3$ and $CH_3NH_3PbI_3$ perovskite devices. Negative scan and positive scan direction were shown to identify the hysteresis behavior in both devices. (d) Comparison of the photocurrent density as a function of time for the two devices held at a forward bias of maximum output power point. The cell was placed in the dark prior to the start of the measurement.

are shown in Figure 3. Similar absorption edges at around 950 nm are observed for all samples, consistent with the same crystalline structure of the resultant perovskite films after thermal annealing. However, note the red-shift of the absorption spectrum of the DMSO and NMP samples in the long wavelength 750−950 nm range versus the DMF sample. This red-shift of absorbance correlates well with the observed crystal size, which is consistent with several recent studies on the perovskite photoluminescence spectra.[40,41] In these studies, small perovskite crystallites exhibit blue-shifted emission relative to large crystals. The optical absorption coefficient (α/S) was calculated using reflectance data according to the Kubelka−Munk equation,[42] $\alpha/S = (1 - R)^2/2R$, where R is the percentage of reflected light and α and S are the absorption and scattering coefficients, respectively. The DMSO solvent-derived films have a similar optical band gap edge compared to DMF-derived films (~1.3 eV), but with a steeper slope in the absorption, suggesting a higher absorption coefficient.

Heterojunction Solar Cell Fabrication and Performance. The present high-quality perovskite films were incorporated into a TiO_2-based heterojunction depleted device structure, which is free of hole transporting materials (HTMs) such as the commonly used spiro-OMeTAD.[18−20] A schematic of the heterojunction depleted device is shown in Figure 4a, in which the perovskite layer acts as a light absorber and also a hole transporting material. One important reason to exclude the HTM with these $CH_3NH_3SnI_3$ perovskite films is the incompatibility, recognized by us and other groups, of the tin perovskite and additives generally added to increase the hole mobility of the pristine spiro-OMeTAD, such as 4-*tert*-butylpyridine and hydrophilic lithium bis(trifluoromethane)-sulfonimide.[10,27] In this study, a compact TiO_2 layer with a thickness around 50 nm was first deposited on a pre-etched FTO substrate to reduce carrier recombination. A 200 nm mesoporous TiO_2nanocrystalline layer was then cast on top to serve as the electron transporting layer. The perovskite layer was next spin-coated on top of the mesoporous TiO_2 layer using a 1.0 M DMSO solution of $CH_3NH_3SnI_3$. Note that 20 mol % SnF_2 was added to the solution to decrease the conductivity of the $CH_3NH_3SnI_3$ layer according to our previous work.[43] Recent work also shows that SnF_2 addition is important to decrease Sn vacancies in the $CsSnI_3$ perovskite system.[44] The device was completed by thermal evaporation of a 100 nm gold electrode on top under a vacuum up to 10^{-5} Torr. All devices were assembled in a N_2-filled glovebox and were quickly transferred to the thermal evaporator, hence minimizing exposure to air ~5 min. Encapsulation was subsequently performed under the same conditions using a hot melt polymer (Surlyn film from DuPont) laminate with a glass coverslip. This encapsulation was done to protect the devices against O_2 or moisture after fabrication. The sealed cells were next removed from the glovebox and immediately measured in air. Control devices using DMF solvent-derived perovskite films were fabricated under the same conditions. A depleted heterojunction device with $CH_3NH_3PbI_3$ was also fabricated in the absence of HTM material, without encapsulation. The $CH_3NH_3PbI_3$ perovskite layer was deposited using the conventional sequential deposition method.[19,22] Device photovoltaic performance characteristics are presented in Figure 4b.

DOI: 10.1021/jacs.5b06658
J. Am. Chem. Soc. XXXX, XXX, XXX−XXX

It should be mentioned that all $CH_3NH_3SnI_3$ devices fabricated with DMF as the solvent suffered short circuits. We attribute this to the inevitable voids or film defects formed during the spin-coating process, as shown in Figure 3a. These voids or pinholes would lead to direct contact between the top electrode and the FTO substrate, causing shorting of these devices. In contrast, the DMSO solution derived perovskite films effectively avoid device shorting, primarily owing to the ultrasmooth pinhole-free film morphology and low doping state of the tin perovskite. These devices show an unprecedented short-circuit photocurrent density of 21.4 mA cm^{-2}, albeit with a modest open-circuit photovoltage of 320 mV and a fill factor of 0.46. The overall power conversion efficiency is calculated to be 3.15%. The photovoltaic performance obtained is substantially lower than that of the $CH_3NH_3PbI_3$ counterpart with the same device structure, which shows a short-circuit photocurrent density of 15.2 mA cm^{-2}, an open-circuit photovoltage of 668 mV, and a fill factor of 0.57, corresponding to a power conversion efficiency of 5.79%. The limited photovoltaic performance for this HTM-free heterojunction device could originate from loss of the light harvesting in the long wavelength region as well as the interfacial charge recombination loss at the perovskite interface.[19] The smaller open-circuit photovoltage for the $CH_3NH_3SnI_3$ cell may originate from the lower conduction band edge (4.17 eV) compared to that of lead analogue (3.93 eV) as measured in our previous report.[28] However, other factors may play a role such as higher background carrier density. The higher photocurrent density in the $CH_3NH_3SnI_3$ device is consistent with the smaller optical band gap (1.3 eV) and therefore a wider light harvesting range than the lead analogue (1.55 eV), which is corroborated with the incident-photon-to-current conversion efficiency (IPCE) spectra shown in Figure 4c. The devices with DMSO-derived $CH_3NH_3SnI_3$ films show photocurrent response up to 950 nm, which is almost 150 nm red-shifted compared with $CH_3NH_3PbI_3$ device. Integrating the overlap of the IPCE spectrum with the AM 1.5G solar photon flux yields a photocurrent density of 20.58 and 15.17 mA cm^{-2} for the tin and lead halide perovskite films, respectively, which is in excellent agreement with the measured photocurrent densities. This confirms the negligible mismatch between the simulated sunlight and the AM 1.5G standard.

Since the notorious photocurrent hysteresis presents a major issue during characterization of device efficiency in lead perovskites,[45−47] we measured the photovoltaic response by reversing the scanning direction in our cells. No noticeable hysteresis is observed with different scanning directions for the $CH_3NH_3SnI_3$ perovskite solar cell in Figure 4b. A small shift in V_{oc} was noticed when switching the scanning direction for the $CH_3NH_3PbI_3$ device. This hysteresis agrees well with the previous reports of lead perovskite solar cells and has been speculated to originate from various causes including trapping/detrapping of charge carriers,[46] changes in absorber or contact conductivity,[48] ferroelectricity,[49] and ion migration.[50] In order to verify the measured photocurrent density, we also measured the steady-state photocurrent output at the maximum power point. As shown in Figure 4d, the photocurrent rapidly saturates, and the steady-state current is found to be stable at 16.8 mA cm^{-2} for the entire measurement period of 300 s. However, a slight decay on the photocurrent density in the lead perovskite heterojunction device is observed within the first hundred seconds under illumination, which then stabilizes for the entire testing period. Such a photocurrent density decay could originate from defects near the surface of perovskite or interface states specifically generated from the solution processing.[51] The relatively stable steady-state photocurrent response in the $CH_3NH_3SnI_3$ device further confirms the high quality and low level of electronic disorder in the perovskite layer.

Charge Extraction and Transient Photovoltage Measurements. To further understand the photovoltaic differences between the lead and tin perovskite solar cells, charge extraction and transient photovoltage measurements were performed to investigate the underlying carrier dynamics along the entire pathway in the completed solar cells. The carrier density in the devices under operational conditions with different light intensities was first probed by the charge extraction method.[52−54] Figure 5a shows the charge extraction curves for the $CH_3NH_3SnI_3$ devices under different incident light intensities. The exponential fitting curves are also presented. Note that the initial steady-state starting condition is from short circuit. The dependence of the carrier concentration on the illuminating light intensity for the two types of perovskite solar cells is shown in Figure 5b. Typically, the carrier density shows an exponential increase with the incident light intensity in both devices as an increasing number of injected electrons are stored in the perovskite films. The stored charge follows Boltzmann statistics, which results in accumulation and carrier diffusion dominated dynamics. The $CH_3NH_3PbI_3$ device generates a carrier density of the order of 10^{16} cm^{-3} under white LED illumination. Impressively, the

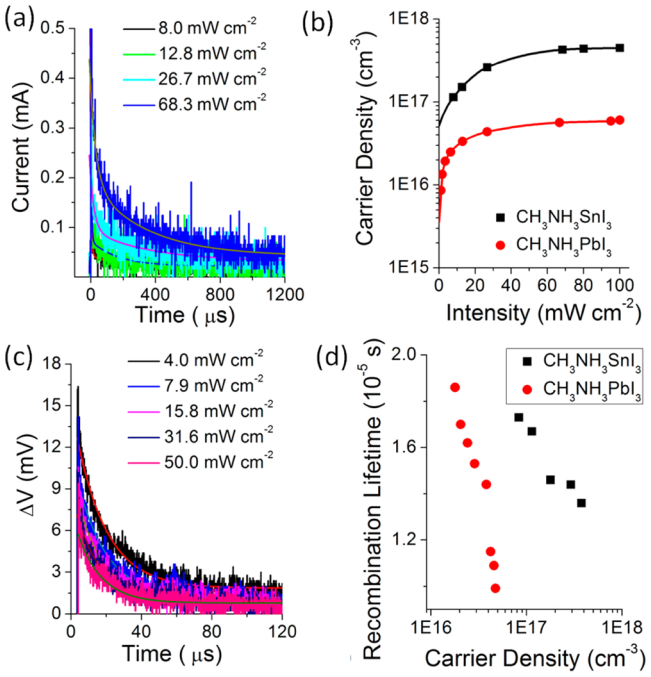

Figure 5. (a) Representative charge extraction curves for the $CH_3NH_3SnI_3$ devices under different incident light intensity. (b) Comparison of the integrated carrier density as a function of light intensity for the $CH_3NH_3SnI_3$ and $CH_3NH_3PbI_3$ devices from the charge extraction measurements. (c) Typical transient photovoltage decay curves for the $CH_3NH_3SnI_3$ devices as a function of light intensity. The exponential fitted curves are also shown in both cases. (d) Recombination lifetime derived from the transient photovoltage decay curves as a function of the carrier density in the operational devices for $CH_3NH_3SnI_3$ and $CH_3NH_3PbI_3$ devices.

DOI: 10.1021/jacs.5b06658
J. Am. Chem. Soc. XXXX, XXX, XXX−XXX

light-induced carrier density for the $CH_3NH_3SnI_3$ counterpart is 1 order of magnitude higher than the lead device, which is attributed to the higher J_{SC} observed in the corresponding $J-V$ curves (Figure 4b). The photocarrier charge density obtained can be traced back to the intrinsic properties of the $CH_3NH_3PbI_3$ and $CH_3NH_3SnI_3$ perovskites, which was shown previously by Hall effect measurements have a dark carrier density of $\sim 10^9-10^{11}$ cm^{-3} and $\sim 10^{14}-10^{17}$ cm^{-3} for $CH_3NH_3PbI_3$ and for semiconducting $CH_3NH_3SnI_3$, respectively. The "background" dark carrier density of the Sn-based perovskite is thus responsible for the lower photovoltaic efficiency in comparison with the Pb-based analogues.

Small perturbation transient photovoltage measurements were next employed to derive the recombination lifetime in the perovskite absorber layer and to gather information on carrier recombination rates in the working device.[56,57] Representative transient photovoltage curves for both devices are shown in Figure 5c. The apparent lifetime of photogenerated carriers (τ) can be evaluated by fitting the transient decay to an exponential function. Details of the fitting curves are shown in the Figures S6 and S7. Figure 5d shows the apparent recombination lifetime as a function of carrier density derived from the charge extraction. The recombination lifetime decreases with carrier density in the device due to intercarrier collisions and the larger driving force for charge recombination. Unexpectedly, these two devices showed comparable recombination lifetime in the range of 10−20 μs. However, a notable carrier density difference is observed, which is attributable to the different V_{oc} in the $J-V$ curves and possibly derives from the different recombination mechanisms between $CH_3NH_3PbI_3$ and $CH_3NH_3SnI_3$. Note that our devices showed substantially longer recombination lifetimes compared to the several microseconds for the recent high-efficiency $CH_3NH_3PbI_3$ devices with a hole-transporting layer.[58] A similar trend was also reported in a recent study comparing the interfacial charge transfer mechanism in both p−n heterojunction and p−i−n device architectures.[59] The additional recombination pathways between the excited electrons in the perovskite layer and holes in hole-transporting materials were ascribed to the shorter carrier lifetimes in the p−i−n devices with a spiro-OMeTAD layer.[59] As for the difference between the $CH_3NH_3SnI_3$ and $CH_3NH_3PbI_3$ devices in our study, we observe that the slopes of the carrier lifetimes in Figure 5d are quite different, thus reflecting the different recombination kinetics in these devices. This is reasonable due to the significant mobility differences in the two perovskite materials as shown in our previous reports.[28,55] Another reason may be associated with the different defect distribution profiles in the two perovskites.[60−62]

Further investigations on this issue using electrochemical impedance analyses and transient photoluminescence spectroscopy are underway in our group.

CONCLUSIONS

In summary, solvent effects on the crystallization process for $CH_3NH_3SnI_3$ perovskite films has been investigated and compared in single-step solution processes. The solvent-induced intermediate phase plays an important role in controlling the crystallization process and final thin film quality. The stabilization of the intermediate SnI_2 solvates prior to the formation of the perovskite films is found to promote homogeneous nucleation and enables an adjustable perovskite film growth rate. High-quality, pinhole-free $CH_3NH_3SnI_3$ films are achieved using DMSO and NMP as solvents and afford lead-free perovskite heterojunction depleted solar cells without a hole-transporting material layer. An unprecedented photocurrent density of up to 21 mA cm^{-2} is obtained while charge extraction and transient photovoltage decay measurements reveal comparable recombination lifetimes in the $CH_3NH_3PbI_3$ and $CH_3NH_3SnI_3$ devices. The tin perovskite device exhibits 1 order of magnitude higher photocarrier density with respect to the lead analogue as a result of its higher dark carrier density. These results suggest that the Sn-based devices can be used as efficient alternatives for the Pb-based devices provided the "background" carrier density can be reduced to intrinsic levels. This expectation derives from the fact that semiconductors with similar band gaps to $CH_3NH_3SnI_3$, such as InP (E_g = 1.34 eV), are capable of intrinsic "background" carrier densities as low as 10^7 cm^{-3}.[63] Therefore, future efforts should focus on ways to decrease the background carrier density in $CH_3NH_3SnI_3$. We can then expect devices with efficiencies greater than 15%, approaching those of the venerable $CH_3NH_3PbI_3$ perovskite.

ASSOCIATED CONTENT

Supporting Information

The Supporting Information is available free of charge on the ACS Publications website at DOI: 10.1021/jacs.5b06658.

Detailed experimental procedures and crystalline structure information on the DMSO solvation intermediates (SnI_2·3DMSO), Figures S1−S7 and Tables S1−S5 (PDF)

Structure of SnI_2·3DMSO (CIF)

AUTHOR INFORMATION

Corresponding Author

*E-mail m-kanatzidis@northwestern.edu.

Notes

The authors declare no competing financial interest.

ACKNOWLEDGMENTS

This research was supported as part of the ANSER Center, an Energy Frontier Research Center funded by the U.S Department of Energy, Office of Science, Office of Basic Energy Sciences, under Award DE-SC0001059. Electron microscopy analysis was done through the use of the EPIC facility (NUANCE Center, Northwestern University), which has received support from the MRSEC program (NSF DMR-1121262) at the Materials Research Center, and the Nanoscale Science and Engineering Center (EEC-0118025/003), both programs of the National Science Foundation, the state of Illinois, and Northwestern University.

REFERENCES

(1) Nayak, P. K.; Cahen, D. *Adv. Mater.* **2014**, *26*, 1622.
(2) Kazim, S.; Nazeeruddin, M. K.; Gratzel, M.; Ahmad, S. *Angew. Chem., Int. Ed.* **2014**, *53*, 2812.
(3) Lotsch, B. V. *Angew. Chem., Int. Ed.* **2014**, *53*, 635.
(4) Wei, Z. H.; Chen, H. N.; Yan, K. Y.; Yang, S. H. *Angew. Chem., Int. Ed.* **2014**, *53*, 13239.
(5) Borriello, I.; Cantele, G.; Ninno, D. *Phys. Rev. B: Condens. Matter Mater. Phys.* **2008**, *77*, 235214.
(6) Mitzi, D. B. *Prog. Inorg. Chem.* **1999**, *48*, 1.
(7) Kagan, C. R.; Mitzi, D. B.; Dimitrakopoulos, C. D. *Science* **1999**, *286*, 945.
(8) Zhang, Q. C.; Liu, X. G. *Small* **2012**, *8*, 3711.
(9) Noh, J. H.; Im, S. H.; Heo, J. H.; Mandal, T. N.; Seok, S. I. *Nano Lett.* **2013**, *13*, 1764.

DOI: 10.1021/jacs.5b06658
J. Am. Chem. Soc. XXXX, XXX, XXX−XXX

(10) Hao, F.; Stoumpos, C. C.; Cao, D. H.; Chang, R. P. H.; Kanatzidis, M. G. *Nat. Photonics* **2014**, *8*, 489.
(11) Heo, J. H.; Im, S. H.; Noh, J. H.; Mandal, T. N.; Lim, C. S.; Chang, J. A.; Lee, Y. H.; Kim, H. J.; Sarkar, A.; Nazeeruddin, M. K.; Gratzel, M.; Seok, S. I. *Nat. Photonics* **2013**, *7*, 486.
(12) Xing, G. C.; Mathews, N.; Sun, S. Y.; Lim, S. S.; Lam, Y. M.; Gratzel, M.; Mhaisalkar, S.; Sum, T. C. *Science* **2013**, *342*, 344.
(13) Stranks, S. D.; Eperon, G. E.; Grancini, G.; Menelaou, C.; Alcocer, M. J. P.; Leijtens, T.; Herz, L. M.; Petrozza, A.; Snaith, H. J. *Science* **2013**, *342*, 341.
(14) Wojciechowski, K.; Saliba, M.; Leijtens, T.; Abate, A.; Snaith, H. J. *Energy Environ. Sci.* **2014**, *7*, 1142.
(15) Lee, M. M.; Teuscher, J.; Miyasaka, T.; Murakami, T. N.; Snaith, H. J. *Science* **2012**, *338*, 643.
(16) Liu, M. Z.; Johnston, M. B.; Snaith, H. J. *Nature* **2013**, *501*, 395.
(17) Liu, D. Y.; Kelly, T. L. *Nat. Photonics* **2014**, *8*, 133.
(18) Etgar, L.; Gao, P.; Xue, Z. S.; Peng, Q.; Chandiran, A. K.; Liu, B.; Nazeeruddin, M. K.; Gratzel, M. *J. Am. Chem. Soc.* **2012**, *134*, 17396.
(19) Hao, F.; Stoumpos, C. C.; Liu, Z.; Chang, R. P. H.; Kanatzidis, M. G. *J. Am. Chem. Soc.* **2014**, *136*, 16411.
(20) Mei, A. Y.; Li, X.; Liu, L. F.; Ku, Z. L.; Liu, T. F.; Rong, Y. G.; Xu, M.; Hu, M.; Chen, J. Z.; Yang, Y.; Gratzel, M.; Han, H. W. *Science* **2014**, *345*, 295.
(21) Kojima, A.; Teshima, K.; Shirai, Y.; Miyasaka, T. *J. Am. Chem. Soc.* **2009**, *131*, 6050.
(22) Burschka, J.; Pellet, N.; Moon, S. J.; Humphry-Baker, R.; Gao, P.; Nazeeruddin, M. K.; Gratzel, M. *Nature* **2013**, *499*, 316.
(23) Zhou, H.; Chen, Q.; Li, G.; Luo, S.; Song, T.-b.; Duan, H.-S.; Hong, Z.; You, J.; Liu, Y.; Yang, Y. *Science* **2014**, *345*, 542.
(24) Mathew, S.; Yella, A.; Gao, P.; Humphry-Baker, R.; Curchod, B. F. E.; Ashari-Astani, N.; Tavernelli, I.; Rothlisberger, U.; Nazeeruddin, M. K.; Gratzel, M. *Nat. Chem.* **2014**, *6*, 242.
(25) Liu, Y. S.; Chen, C. C.; Hong, Z. R.; Gao, J.; Yang, Y.; Zhou, H. P.; Dou, L. T.; Li, G.; Yang, Y. *Sci. Rep.* **2013**, *3*, 3356.
(26) Green, M. A.; Emery, K.; Hishikawa, Y.; Warta, W.; Dunlop, E. D. *Prog. Photovoltaics* **2014**, *22*, 701.
(27) Noel, N. K.; Stranks, S. D.; Abate, A.; Wehrenfennig, C.; Guarnera, S.; Haghighirad, A. A.; Sadhanala, A.; Eperon, G. E.; Pathak, S. K.; Johnston, M. B.; Petrozza, A.; Herz, L. M.; Snaith, H. J. *Energy Environ. Sci.* **2014**, *7*, 3061.
(28) Hao, F.; Stoumpos, C. C.; Chang, R. P. H.; Kanatzidis, M. G. *J. Am. Chem. Soc.* **2014**, *136*, 8094.
(29) Liang, K. N.; Mitzi, D. B.; Prikas, M. T. *Chem. Mater.* **1998**, *10*, 403.
(30) Wu, Y. Z.; Islam, A.; Yang, X. D.; Qin, C. J.; Liu, J.; Zhang, K.; Peng, W. Q.; Han, L. Y. *Energy Environ. Sci.* **2014**, *7*, 2934.
(31) Zhao, Y. X.; Zhu, K. *J. Phys. Chem. C* **2014**, *118*, 9412.
(32) Jeon, N. J.; Noh, J. H.; Kim, Y. C.; Yang, W. S.; Ryu, S.; Il Seol, S. *Nat. Mater.* **2014**, *13*, 897.
(33) Im, J. H.; Jang, I. H.; Pellet, N.; Gratzel, M.; Park, N. G. *Nat. Nanotechnol.* **2014**, *9*, 927.
(34) Eperon, G. E.; Burlakov, V. M.; Docampo, P.; Goriely, A.; Snaith, H. J. *Adv. Funct. Mater.* **2014**, *24*, 151.
(35) Zhang, S. J.; Audebert, P.; Wei, Y.; Al Choueiry, A.; Lanty, G.; Brehier, A.; Galmiche, L.; Clavier, G.; Boissiere, C.; Lauret, J. S.; Deleporte, E. *Materials* **2010**, *3*, 3385.
(36) Miyamae, H.; Numahata, Y.; Nagata, M. *Chem. Lett.* **1980**, *9*, 663.
(37) Shi, D.; Adinolfi, V.; Comin, R.; Yuan, M.; Alarousu, E.; Buin, A.; Chen, Y.; Hoogland, S.; Rothenberger, A.; Katsiev, K.; Losovyj, Y.; Zhang, X.; Dowben, P. A.; Mohammed, O. F.; Sargent, E. H.; Bakr, O. M. *Science* **2015**, *347*, 519.
(38) Sheldrick, G. M. *Acta Crystallogr., Sect. A: Found. Crystallogr.* **2008**, *64*, 112.
(39) Nie, W. Y.; Tsai, H. H.; Asadpour, R.; Blancon, J. C.; Neukirch, A. J.; Gupta, G.; Crochet, J. J.; Chhowalla, M.; Tretiak, S.; Alam, M. A.; Wang, H. L.; Mohite, A. D. *Science* **2015**, *347*, 522.
(40) De Bastiani, M.; D'Innocenzo, V.; Stranks, S. D.; Snaith, H. J.; Petrozza, A. *APL Mater.* **2014**, *2*, 081509.
(41) Zhang, W.; Saliba, M.; Moore, D. T.; Pathak, S. K.; Horantner, M. T.; Stergiopoulos, T.; Stranks, S. D.; Eperon, G. E.; Alexander-Webber, J. A.; Abate, A.; Sadhanala, A.; Yao, S. H.; Chen, Y. L.; Friend, R. H.; Estroff, L. A.; Wiesner, U.; Snaith, H. J. *Nat. Commun.* **2015**, *6*, 6142.
(42) Gate, L. F. *Appl. Opt.* **1974**, *13*, 236.
(43) Chung, I.; Lee, B.; He, J. Q.; Chang, R. P. H.; Kanatzidis, M. G. *Nature* **2012**, *485*, 486.
(44) Kumar, M. H.; Dharani, S.; Leong, W. L.; Boix, P. P.; Prabhakar, R. R.; Baikie, T.; Shi, C.; Ding, H.; Ramesh, R.; Asta, M.; Graetzel, M.; Mhaisalkar, S. G.; Mathews, N. *Adv. Mater.* **2014**, *26*, 7122.
(45) Unger, E. L.; Hoke, E. T.; Bailie, C. D.; Nguyen, W. H.; Bowring, A. R.; Heumuller, T.; Christoforo, M. G.; McGehee, M. D. *Energy Environ. Sci.* **2014**, *7*, 3690.
(46) Snaith, H. J.; Abate, A.; Ball, J. M.; Eperon, G. E.; Leijtens, T.; Noel, N. K.; Stranks, S. D.; Wang, J. T. W.; Wojciechowski, K.; Zhang, W. *J. Phys. Chem. Lett.* **2014**, *5*, 1511.
(47) Wei, J.; Zhao, Y. C.; Li, H.; Li, G. B.; Pan, J. L.; Xu, D. S.; Zhao, Q.; Yu, D. P. *J. Phys. Chem. Lett.* **2014**, *5*, 3937.
(48) Staebler, D. L.; Wronski, C. R. *J. Appl. Phys.* **1980**, *51*, 3262.
(49) Dualeh, A.; Moehl, T.; Tetreault, N.; Teuscher, J.; Gao, P.; Nazeeruddin, M. K.; Gratzel, M. *ACS Nano* **2014**, *8*, 4053.
(50) Tress, W.; Marinova, N.; Moehl, T.; Zakeeruddin, S. M.; Nazeeruddin, M. K.; Gratzel, M. *Energy Environ. Sci.* **2015**, *8*, 995.
(51) Kim, H. S.; Park, N. G. *J. Phys. Chem. Lett.* **2014**, *5*, 3434.
(52) Shuttle, C. G.; Maurano, A.; Hamilton, R.; O'Regan, B.; de Mello, J. C.; Durrant, J. R. *Appl. Phys. Lett.* **2008**, *93*, 183501.
(53) Duffy, N. W.; Peter, L. M.; Rajapakse, R. M. G.; Wijayantha, K. G. U. *Electrochem. Commun.* **2000**, *2*, 658.
(54) Shuttle, C. G.; Hamilton, R.; O'Regan, B. C.; Nelson, J.; Durrant, J. R. *Proc. Natl. Acad. Sci. U. S. A.* **2010**, *107*, 16448.
(55) Stoumpos, C. C.; Malliakas, C. D.; Kanatzidis, M. G. *Inorg. Chem.* **2013**, *52*, 9019.
(56) Mora-Sero, I.; Dittrich, T.; Garcia-Belmonte, G.; Bisquert, J. *J. Appl. Phys.* **2006**, *100*, 103705.
(57) O'Regan, B. C.; Bakker, K.; Kroeze, J.; Smit, H.; Sommeling, P.; Durrant, J. R. *J. Phys. Chem. B* **2006**, *110*, 17155.
(58) Zhou, H. P.; Chen, Q.; Li, G.; Luo, S.; Song, T. B.; Duan, H. S.; Hong, Z. R.; You, J. B.; Liu, Y. S.; Yang, Y. *Science* **2014**, *345*, 542.
(59) Xu, X. B.; Zhang, H.; Cao, K.; Cui, J.; Lu, J. F.; Zeng, X. W.; Shen, Y.; Wang, M. K. *ChemSusChem* **2014**, *7*, 3088.
(60) Yin, W. J.; Shi, T. T.; Yan, Y. F. *Appl. Phys. Lett.* **2014**, *104*, 063903.
(61) Kim, J.; Lee, S. H.; Lee, J. H.; Hong, K. H. *J. Phys. Chem. Lett.* **2014**, *5*, 1312.
(62) Agiorgousis, M. L.; Sun, Y. Y.; Zeng, H.; Zhang, S. B. *J. Am. Chem. Soc.* **2014**, *136*, 14570.
(63) In *Group IV Elements, IV-IV and III-V Compounds. Part b - Electronic, Transport, Optical and Other Properties*; Madelung, O., Rössler, U., Schulz, M., Eds.; Springer: Berlin, 2002; Vol. *41A1b*, p 1.
(64) Reichardt, C.; Welton, T. In *Solvents and Solvent Effects in Organic Chemistry*; Wiley-VCH Verlag GmbH & Co. KGaA: Weinheim, 2010; p 549.

DOI: 10.1021/jacs.5b06658
J. Am. Chem. Soc. XXXX, XXX, XXX−XXX